

PAPER • OPEN ACCESS

## Uncertainty analysis in structured laser illumination planar imaging (SLIPI) applied to non-linear signals: gas-phase phosphor thermometry

To cite this article: Luming Fan and Simone Hochgreb 2019 *Meas. Sci. Technol.* **30** 084003

View the [article online](#) for updates and enhancements.

You may also like

- [Multiple scattering reduction in instantaneous gas phase phosphor thermometry: applications with dispersed seeding](#)

Michael Stephan, Florian Zentgraf, Edouard Berrocal et al.

- [A flight-phase terrain following control strategy for stable and robust hopping of a one-legged robot under large terrain variations](#)

Natan Shemer and Amir Degani

- [Magnetic configuration effects on TAE-induced losses and a comparison with the orbit-following model in the Large Helical Device](#)

Kunihiro Ogawa, Mitsutaka Isobe, Kazuo Toi et al.

# Uncertainty analysis in structured laser illumination planar imaging (SLIPI) applied to non-linear signals: gas-phase phosphor thermometry

Luming Fan<sup>1</sup>  and Simone Hochgreb<sup>1</sup> 

Hopkinson Laboratory, Department of Engineering, University of Cambridge, Trumpington Street, CB2 1PZ, United Kingdom

E-mail: [lf368@cam.ac.uk](mailto:lf368@cam.ac.uk) (Luming Fan)

Received 30 November 2018, revised 25 March 2019

Accepted for publication 16 April 2019

Published 28 June 2019



## Abstract

Recent studies have used structured laser illumination planar imaging (SLIPI) combined with phosphor thermography to remove multiple scatter effects and near-wall reflections, which lead to biases in temperature measurements and reduced spatial resolution. We show that for the typical non-linear pump-signal range under which thermographic phosphors are used, errors may arise in the reconstruction of the temperature field using SLIPI. In this study, synthetic laser induced phosphorescence (LIP) images are generated numerically by adapting the synthetic PIV image generator for the purpose. The simulations are combined with phosphorescent signal yield functions obtained from experimental data to investigate the application of SLIPI to gas-phase phosphor thermography. We conclude that whilst SLIPI is effective in removing scattering noise for phosphors for which the two-colour signal ratio is insensitive to the laser fluence, it creates a bias in the temperature measurement otherwise. We also show that the extent of multiple scatter in LIP images is always overestimated by SLIPI, owing to the non-linear emission behaviour and particle image diffraction.

Keywords: phosphor thermometry, synthetic LIP image, SLIPI

(Some figures may appear in colour only in the online journal)

## 1. Introduction

### 1.1. Multiple scattering

Multiple scattering is a feature of any experiment involving particles. In particular, the issue of multiple scattering in phosphorescence emission has emerged as a source of error in several studies. The term ‘multiple scattering’ has been used to describe the phenomenon by which photons are scattered

by particles beyond the target region when passing through an optically dense medium before reaching the detector [1], thus contributing to the signal where none should exist. The phenomenon is prevalent in a variety of systems where small particles or droplets are present, notably in dense sprays. For measurement techniques based on image correlation such as PIV, the uncertainty brought by multiple scattering is trivial unless excessive seeding is used. However, for laser-induced phosphorescence (LIP), multiple scattering may have a more significant influence on temperature measurements. As a technique relying on the intensity ratio of the observed signal, multiple scattering may affect the measurements via several different mechanisms [2] illustrated in figure 1, and summarised as follows:

<sup>1</sup> Author to whom any correspondence should be addressed.

 Original content from this work may be used under the terms of the [Creative Commons Attribution 3.0 licence](#). Any further distribution of this work must maintain attribution to the author(s) and the title of the work, journal citation and DOI.

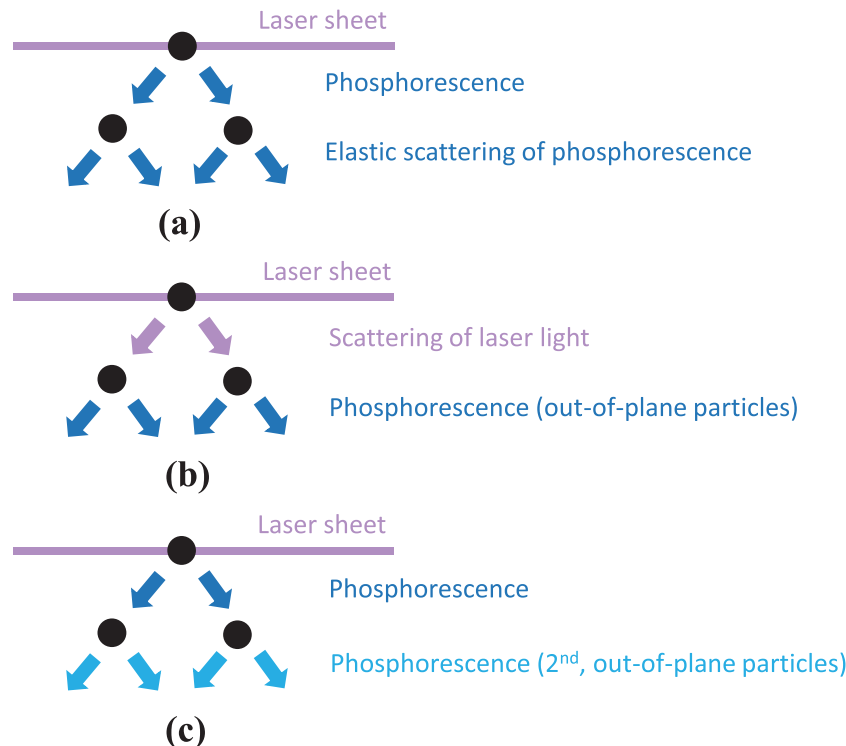


**Figure 1.** Three mechanisms of multiple scattering for phosphorescence: (a) Elastic scattering of the phosphor signal emitted from the measurement plane; (b) excitation of phosphors by the scattered laser light; and (c) preferential re-absorption and secondary emission. The black solid circles represent phosphor particles.

- (a) Elastic scattering of the phosphor signal emitted from the measurement plane.** In this scenario, the spatial resolution is affected, leading to blurred images. If the spatial resolution significantly deteriorates, the temperature measurements could also be biased. For example, some photons originated from the cold co-flow may be scattered towards the central hot jet, and then captured by the cameras.
- (b) Excitation of phosphors by the scattered laser light.** Laser light scattered by in-plane particles excites the out-of-plane particles. Hence the signal captured by the detector conveys both in-plane and out-of-plane temperature information.
- (c) Preferential re-absorption and secondary emission.** The excitation and emission spectra of some phosphorescent tracers may partially overlap, and the photons in the overlapping spectral range emitted from the laser plane may be re-absorbed by particles outside the excitation plane and lead to a secondary emission, which may carry different temperature information, yet contribute to the total signal.

An early report on the multiple scatter effect for phosphor particles in dispersed form [2] showed how the phosphor signal could also be captured from outside the illuminated area by a trimmed laser sheet, suggesting that multiple scattering leads to reduced spatial resolution. Similar phenomena were also reported by [3, 4] where the phosphorescence signal appeared in unseeded regions where no signal should have been found. A recent paper investigated the effects of multiple scattering on a film-cooling application [4] in which a 3 mm

hot jet was injected into a 40 mm cross-flow at an angle, both seeded with BAM:Eu<sup>2+</sup>. Under these conditions, the effect of multiple scattering was estimated to be responsible for a bias in the jet temperature by a striking ~40 K out of 445 K. In the same work, it was reported that the seeding density within the cross-flow should be ten times lower than that in the jet so as to create an unbiased measurement. However, both signal to noise ratio and spatial resolution severely deteriorate at such low seeding rates. The experiments in [3, 5] proved the fact that, in cases where the signal ratio changes with seeding density, a large temperature bias arises. In particular, if preferential re-absorption occurs, the temperature uncertainty also increases with a longer optical path [6]. Hence for large flow configurations, only controlling the seeding density may not be enough to eliminate the effects of multiple scattering. To solve this problem, it was suggested by [6] that an *in situ* calibration at exactly the same seeding density and flow condition would, in principle, allow a compensation for the effects of multiple scattering, although this may not always be possible for internal flows.

## 1.2. SLIPI

**1.2.1. SLIPI theory.** An alternative solution to multiple scattering in laser-induced phosphorescence is to combine it with structured laser illumination planar imaging (SLIPI), as demonstrated by Zentgraf and co-workers [4]. In that work, near-wall effects and multiple-scatter interference was successfully removed from the phosphorescence signal originating from the laser plane. SLIPI works by reconstructing the signal from

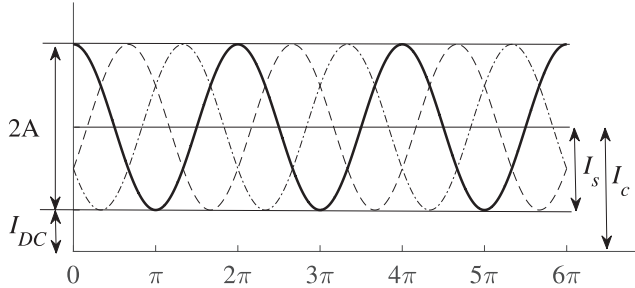


**Figure 2.** Schematic diagram of three modulated harmonic sub-signals in non-dimensional space, showing the corresponding reconstructed signals.

multiple (usually three) sinusoidal spatially modulated laser profiles with phase shift angles  $0, 2\pi/3, 4\pi/3$ , respectively, to illuminate the test area. The assumption is that photons that have been scattered several times or produced during the secondary emission do not preserve the spatial modulation, the true signal can be reconstructed from the modulated fraction, whilst the unmodulated fraction is viewed as scattered signal which does not originate from modulated incident light sheet. The three modulated subimages yield signal intensities ( $I_1, I_2$  and  $I_3$ ) can be represented by the following general expression

$$I_i = I_{DC} + I_{AC} = I_{DC} + A[\cos(2\pi\nu y + \Phi_i) + 1] \quad (1)$$

where  $I_{DC}$  (direct current) denotes multiple scattering or any other unmodulated signals, which are assumed to be proportional to the total laser energy passing through the Ronchi grating;  $I_{AC}$  (alternating current) is the modulated signal from the measurement plane;  $A$  is the amplitude of modulation;  $\nu$  the frequency of Ronchi grating. The three sub-signals are sketched in figure 2. The reconstructed clean image without multiple scattering is extracted by calculating

$$I_s = \frac{\sqrt{2}}{3} [(I_1 - I_2)^2 + (I_1 - I_3)^2 + (I_2 - I_3)^2]^{1/2} = A \quad (2)$$

where  $I_s$  is referred to in the literature as the SLIPI image. Meanwhile, previous literature introduced the nomenclature of a conventional image  $I_c$ :

$$I_c = \frac{I_1 + I_2 + I_3}{3} = A + I_{DC}. \quad (3)$$

In the work by Kristensson *et al* [7], the multiple scattering fraction  $\phi$  was defined as

$$\phi = \frac{I_{DC}}{A + I_{DC}} = \frac{I_c - I_s}{I_c} \quad (4)$$

which was used to quantify the relative amount of light being suppressed by SLIPI, or the contribution from multiple scattering to the recorded signal. All above SLIPI analyses hinge on the assumption that the three input sub-signals generated are strictly *harmonic*, and that the signal behaves *linearly* with laser intensity.

**1.2.2. Previous work on SLIPI.** SLIPI has been applied to remove scattering or other uncorrelated noise for extracting Mie scattering images in sprays [1], 2D laser-induced fluorescence (LIF) [8], planar droplet sizing [9] and Rayleigh

thermometry [10]. For studies based on averaged or steady-state images, a single laser with a Ronchi (harmonically modulated) grating that can be traversed vertically is sufficient to perform SLIPI. Executing SLIPI on individual shots, however, requires three single-pulsed laser beams and cameras triggered in sequence within a very short time interval so as to keep the tracers at the same position for all subimages. To solve this, a simplified two-pulse SLIPI approach has been developed [11] and later a single-pulse approach [12]. However, these are not as robust as the three-pulse SLIPI, because the two-pulse approach intrinsically produces residual streaks on the reconstructed image, which requires the use of a low-pass filter; whilst the single-pulse approach loses high-frequency information during the image reconstruction. In a recent study by Kristensson and Berrocal [13], the spatial resolution of one-pulse SLIPI has been improved by crossing two modulated laser sheets at  $90^\circ$ , named xSLIPI.

It is useful to consider under what conditions SLIPI can be usefully applied to LIP. Based on previous literature and the authors' experience in conducting LIP, the application of SLIPI may be necessary when: (a) reducing seeding density is not an option, for example where temperature gradients are high; (b) the experimental test conditions lead to a large scale seeded co-flow region which may introduce severe multiple scattering; and (c) direct incidence of laser light on surfaces cannot be avoided by adjusting the incidence angle or by other strategies such as using UV-absorptive paint. In other situations, excessive multiple scattering can be more easily avoided by reducing phosphor seeding density, whilst the use of intensifiers ahead of cameras can boost the signal (shot noise may also be amplified though). Tests of LIP on BAM:Eu<sup>2+</sup> [14], YAG:Dy, Er [15], ZnO [6] in a simple air jet, and ZnO in water [16], at a seeding density in the order of  $10^{11}$  particles/m<sup>3</sup> show trivial effects from multiple scattering, whilst achieving a reasonable spatial resolution.

**1.2.3. SLIPI for ratio-based methods: linear operation.** SLIPI has been applied to denoise two-colour, intensity-ratio based techniques such as 2D-LIF [8] and LIF/Mie planar droplet sizing [9, 17]. Considering a linear signal response to laser fluence for a two-colour thermometry at both channels, the signal intensity  $I_{i,\lambda}$  obtained for wavelength  $\lambda$  is given by

$$I_{i,\lambda} = I_{DC} + \underbrace{G(\lambda, T)F}_{I_{AC}} \quad (5)$$

where  $G$  is the gain function and

$$F = F_0[\cos(2\pi\nu y + \Phi_i) + 1] \quad (6)$$

is the local fluence as a function of  $y$ . Since laser extinction is a separate problem from multiple scattering or SLIPI, we do not consider it in the present study, although it could be added to the model without difficulty. After the SLIPI operation

$$I_{s,\lambda} = G(\lambda, T)F_0. \quad (7)$$

The signal ratio between two selected channels gives

$$\frac{I_{s,\lambda_1}}{I_{s,\lambda_2}} = \frac{G(\lambda_1, T)}{G(\lambda_2, T)}. \quad (8)$$

The local temperature can be extracted from the signal ratio according to the above equation, after the effects from the unmodulated signal  $I_{DC}$  have been removed by SLIPI. Mathematically, the application of SLIPI on the ratio-based methods does not create any bias so long as the signal growth is linear with the laser fluence.

**1.2.4. SLIPI signals for ratio-based methods: non-linear operation.** For inelastic scattering phenomena such as fluorescence and phosphorescence, a non-linear signal increase with respect to fluence can usually be observed beyond a certain value of the excitation laser fluence. In the case of phosphorescence, the linear emission regime of most commonly used phosphors is limited to a very low fluence range, which is followed by a gradual saturation. In this scenario, equation (5) is rewritten as

$$I_{i,\lambda} = I_{DC} + \underbrace{G(\lambda, T, F)F}_{I_{AC}}. \quad (9)$$

The gain function  $G$  now brings non-harmonicity to the sub-signal  $I_i$ , since the latter becomes a function of a non-unity power of  $F$ . The harmonic analysis depends on the linearity, and is therefore no longer valid. In the present analysis, we take the gas-phase phosphor thermometry as a background scenario and simulate artificial LIP images incorporated with experimentally obtained response curves to clarify the biases introduced by SLIPI due to non-linear signal response, and how to account for them in the final temperature retrieval.

## 2. Numerical method

### 2.1. PIV Synthetic image generator (SIG)

We use synthetic LIP images generated by a Matlab program adapted from the PIV synthetic image generator (SIG) [18]. SIG was developed as an open-source program and has been widely used as a tool to synthesize PIV image pairs based on a user-defined velocity field. It allocates random positions to individual particles, whose size and intensity information depends on the input particle size distribution, laser profile, and other optical settings. The SIG program is now a standard tool for evaluating advanced PIV algorithms, quantifying uncertainty, or estimating parameters during the experimental design stage. Examples of the application of SIG or similar versions can be found in [19] and [20]. In the present study, the original algorithm is adapted to generate phosphorescent particle images on a single frame based on a user-defined temperature field, rather than Mie scattering, by incorporating measured ZnO phosphorescence responses from the previous experiment described in [21].

### 2.2. Adapted SIG for phosphor particles (LIP-SIG)

In the simulation, we consider particles of characteristic diameter smaller than 2  $\mu\text{m}$ , which are typical of the required short response time to the changes in local temperature and

velocity in turbulent gaseous flows [22]. A particle in this size range is much smaller than a typical pixel pitch size in typical fields of view of the order of several centimetres, with resolutions of the order of tens of micrometres, and thus can be viewed as a point light source. For diffraction-limited lenses, the intensity profile of a point light source projected on the image plane obeys the Airy pattern, which can be approximated as a Gaussian function [23]. Note that the Airy disk theory works for both Mie scattering and phosphorescent emission. The intensity distribution of a single phosphor particle image on the object plane is written as a Gaussian distribution,

$$I_p(r) = A \exp\left(-\frac{r^2}{2\sigma^2}\right) \quad (10)$$

where  $r$  is the distance to the centre point of the light source. In the LIP-SIG method, we assume all particle images are circular, with a diameter  $d_\tau$  (in pixels), defined as  $e^{-2}$  diameter of the particle image intensity distribution, so that

$$\sigma = d_\tau/4. \quad (11)$$

The dimension  $d_\tau$  of diffraction-limited particle images is mainly determined by the optical lenses used in the setup, specifically by the magnification factor  $M_0$  and the  $f$ -number, which are assumed to be the same for all particles in the plane. Other factors such as collected wavelength, characteristics of detector, particle sizes, and so on, could also affect the degree of diffraction to some extent. Here we directly define a particle image size  $d_\tau$ , instead of calculating it from the factors above. However, when using the LIP-SIG program to design an experiment, those factors can be added directly into the code. After pixelization, the intensity of pixel  $[x_i, y_i]$  can be obtained by 2D integration of the Gaussian intensity profile over the pixel,

$$\begin{aligned} I_p[x_i, y_i] &= Kd_p^2 \int_{x_i-f_{rx}/2}^{x_i+f_{rx}/2} \exp\left[-\frac{1}{2}\left(\frac{x-x_p}{d_\tau/4}\right)^2\right] dx \\ &\quad \cdot \int_{y_i-f_{ry}/2}^{y_i+f_{ry}/2} \exp\left[-\frac{1}{2}\left(\frac{y-y_p}{d_\tau/4}\right)^2\right] dy \\ &= \frac{K\pi d_p^2 d_\tau^2}{128} \left[ \operatorname{erf}\left(\frac{x-x_p+f_{rx}/2}{\sqrt{2}d_\tau/4}\right) - \operatorname{erf}\left(\frac{x-x_p-f_{rx}/2}{\sqrt{2}d_\tau/4}\right) \right] \\ &\quad \cdot \left[ \operatorname{erf}\left(\frac{y-y_p+f_{ry}/2}{\sqrt{2}d_\tau/4}\right) - \operatorname{erf}\left(\frac{y-y_p-f_{ry}/2}{\sqrt{2}d_\tau/4}\right) \right] \end{aligned} \quad (12)$$

where  $K$  is a calibration constant;  $(x_p, y_p)$  is the position of the point light source in the non-pixelized coordinate, and  $d_p$  denotes the physical diameter of the particle (in  $\mu\text{m}$ ). The fill ratios  $f_{rx}$  and  $f_{ry}$  indicate the ratio of the sensitive area to the total area of a pixel, determined by the chip architecture, and is a user-defined input parameter in SIG [18]. In equation (12), we follow the assumption made in the original SIG program that the signal strength  $I_p$  is proportional to the square of particle diameter  $d_p$ . Yet for phosphorescence, the relation between particle size and emission strength has not been conclusively determined by experimental studies. Here, particles are assumed to be monodispersed so that the variation in particle size  $d_p$  does not affect the analyses.

In order to save computational time, for each particle we only calculate the pixel intensity within a  $d_\tau \times d_\tau$  region centered at the particle position,

$$\begin{aligned} x_p - \lceil d_\tau / 2 \rceil &\leq x_i \leq x_p + \lceil d_\tau / 2 \rceil; \\ y_p - \lceil d_\tau / 2 \rceil &\leq y_i \leq y_p + \lceil d_\tau / 2 \rceil \end{aligned} \quad (13)$$

as the pixel intensity outside this region is an order of magnitude lower than that of the brightest pixel, which is hence set to zero. The phosphorescence signal is, in general, not sufficiently strong to saturate the CCD sensors, so over-exposure is not considered in the modified LIP-SIG code. The final image intensity is assumed to be a linear sum of the intensity generated by all  $N$  particles at a given location:

$$I[x_i, y_i] = \sum_{n=1}^N I_{p,n}[x_i, y_i]. \quad (14)$$

The number of particles  $N$  is related to the volumetric seeding density  $n_p$  by

$$n_p = N/(A\delta) \quad (15)$$

where  $A$  is the area of the simulated image and  $\delta$  the thickness of the laser sheet. Considering a common level of pixel resolution at 20  $\mu\text{m}/\text{pixel}$  and a 0.3 mm thick laser sheet, 5000 particles on a  $200 \times 200$  pixel simulation area corresponds to a seeding density  $n_p = 1.0 \times 10^{12}$  particles  $\text{m}^{-3}$ . This seeding density is about one order magnitude higher than the normal seeding level for PIV measurements (10–15 particles per window), a condition for which multiple scattering may start to affect LIP measurements [6]. In the original SIG code there is an implicit limit on the seeding density, defined by the speckle mode generated by interference patterns from coherent particle scatter when the seeding density is high. This limit is not expected to appear in LIP images, as phosphorescence emission is incoherent. Hence, the LIP-SIG can be applied to investigate seeding cases even under conditions where severe multiple scattering is most likely to occur.

### 2.3. Emission behaviour dependence on temperature and laser fluence

An experimentally obtained calibration function of phosphorescent emission against temperature and local laser fluence has been built into the LIP-SIG program. For the most commonly used phosphors BAM:Eu<sup>2+</sup> and ZnO, the emission intensity increases with laser fluence before reaching a plateau, and decreases with higher temperature due to thermal quenching. The intensity ratio at two selected wavelengths strongly depends on the local temperature, but was also found to be a weak function of laser fluence [14, 16, 24]. In this numerical study, we use the experimental data on the signal obtained from ZnO previously acquired in [21] to define the response curve  $G(\lambda, T, F)F$  for the phosphorescence signal obtained as a function of temperature  $T$  and fluence  $F$ . Figure 3 shows the response curves measured at 350 K.

Two wavelengths are typically selected for extracting the temperature,  $\lambda_r$  and  $\lambda_b$ , referred as blue ( $b$ ) and red ( $r$ ) channel respectively. The choice is usually driven by the maximum

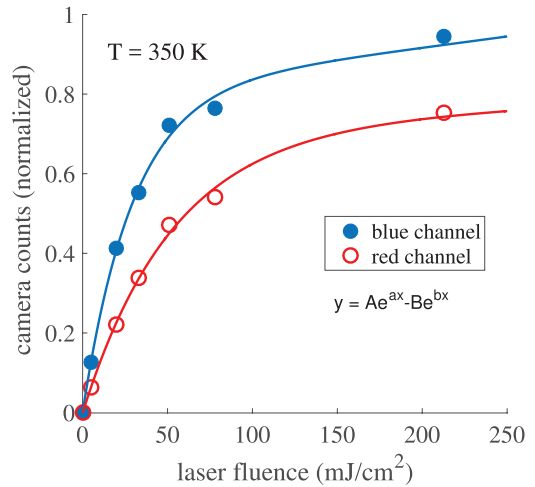


**Figure 3.** Experimentally obtained response curves for ZnO at 350 K. Blue circles are data points collected at the blue channel and red circles at the red channel. The lines show the corresponding two-term exponential fittings of the form  $y = Ae^{ax} - Be^{bx}$ .

sensitivity of the intensity ratio to the temperature, in order to maximize the accuracy of the inversion. For the present response curves, the blue channel spans  $387 \pm 5.5$  nm and the red channel,  $425 \pm 25$  nm. The intensity given by equation (12) at pixel  $[x_i, y_i]$  is assumed to be proportional to the original Gaussian intensity for one particle, local fluence  $F$  and the gain function  $G(\lambda, T, F)F$ ,

$$\begin{aligned} I_{p,\lambda}[x_i, y_i] &= K_0 G(\lambda, T, F)F \\ &\cdot \int_{x_i-1/2}^{x_i+1/2} \exp \left[ -\frac{1}{2} \left( \frac{x - x_p}{d_\tau/4} \right)^2 \right] dx \\ &\cdot \int_{y_i-1/2}^{y_i+1/2} \exp \left[ -\frac{1}{2} \left( \frac{y - y_p}{d_\tau/4} \right)^2 \right] dy \end{aligned} \quad (16)$$

where  $I_{p,\lambda}[x_i, y_i]$  is the intensity at pixel  $[x_i, y_i]$  collected at a given wavelength for a single particle, and the fill ratio  $f_r$  is assumed to be equal to unity for simplicity in both  $x$  and  $y$  directions. The emission intensity was measured for a flow at a constant temperature for a fixed particle concentration, to yield a calibration constant  $K_0$  connecting the measured value corresponding to the sum of particle intensities, on the premise that all monodisperse particles have the same response to the constant temperature and fluence. The pixel intensity for a given particle, collected at a different wavelength, is given as

$$I_{p,r}[x_i, y_i] = R_{rb} I_{p,b}[x_i, y_i] \quad (17)$$

where  $R_{rb}$  is the calibrated signal ratio curve for the red over blue wavelength channels, which is generally also a function of temperature  $T$  and laser fluence  $F$ . Here we must make the assumption that the diffraction pattern captured by the two cameras (red and blue) is identical, even though this may not be the case for real LIP images. Due to slight differences in spatial resolution, angle of light collection, and sub-pixel misalignment of cameras, the same particle image in general appears differently on the two channels. However, in all studies so far, a moving average filter was applied to smooth out discrepancies in the diffraction pattern before the ratio is

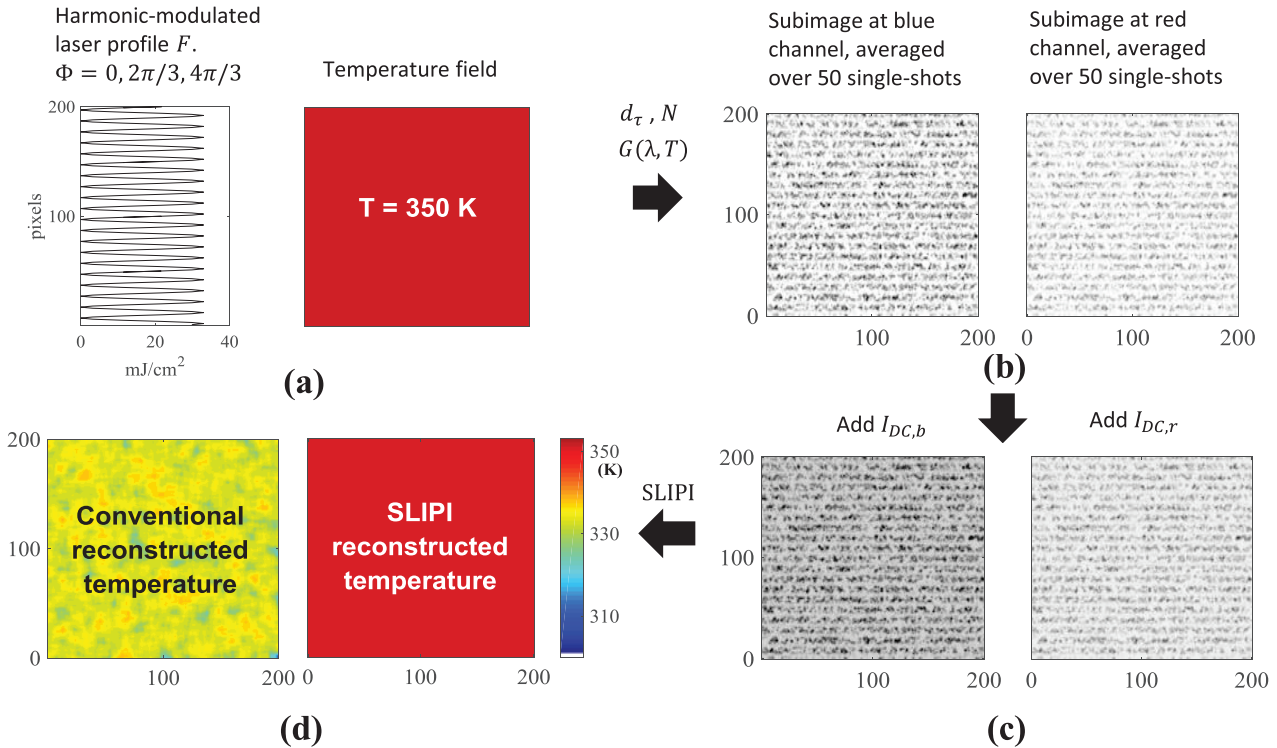


**Figure 4.** Flow chart for SLIPI image synthesis and reconstruction for linear signal behaviour: (a) definition of a modulated laser profile  $F$  and a uniform temperature field (350 K); (b) generation of 50 single-shots SLIPI images ( $200 \times 200$  pixels) using the number of particles ( $N = 5000$ ), using a fixed gain function  $G(\lambda, T)$ ; (c) addition of constant synthetic signals  $I_{DC,b}$  and  $I_{DC,r}$  to the two channels; (d) extraction of temperature field from conventional and SLIPI reconstructed image. As expected, the SLIPI operation corrects the temperature bias caused by intentionally added unmodulated signals  $I_{DC}$ .

taken between the intensity in the two channels, sacrificing spatial resolution for realizability. Therefore the assumption made here does not create effective discrepancies between simulations and real two-colour LIP measurements in gaseous flows.

With these steps, the response of phosphor emission to temperature and laser fluence was built into the LIP-SIG program. The code can now synthesize random pairs of LIP images based on an input laser profiles and temperature field.

#### 2.4. SLIPI subimage generation and image reconstruction

The flowchart in figure 4 schematically describes the process of SLIPI subimage synthesis and recovery. All simulations were conducted over a  $200 \times 200$  pixel area. Three horizontally harmonic-modulated laser profiles  $F(y)$  were defined at phase angles of  $0, 2\pi/3, 4\pi/3$ , respectively. Fifty single shots were synthesized for each case. A total number  $N$  of particles were generated on each single-shot, and a random position  $(x_p, y_p)$  was allocated to each particle. We conducted a convergence study of intensity ratio as a function of number of images averaged for the SLIPI algorithm, as shown in figure 5.  $N$  equals to 500, 2000, and 5000 were used for each single shot. Two cases are considered: in the *individual-shot averaged* case, the intensity ratio is obtained for each particle, corresponding to instantaneous SLIPI where multiple cameras are used in a single shot. In the *ensemble averaged* case, multiple images are averaged first before calculating the average

intensity ratio. In the individual-shot averaged case, the ratio only depends on each particle, and therefore presents a reference case for the present constant temperature field. For the ensemble averaged case, 20 images are sufficient to converge the temperature extraction for  $N = 5000$ . However, for a commonly used PIV seeding level  $N = 500$  ( $\sim 13$  particles per  $32 \times 32$  window), 200 images still do not yet converge the intensity ratio. To be consistent with [4], the present simulations follow the ensemble average routine.

A uniform temperature field of 350 K in the measurement plane was used in this example. For the purpose of demonstration, for this case we assume a linear signal response as equation (5). Based on equations (14), (16) and (17), the three sets of SLIPI subimages were simulated and averaged for both channels, as shown in figure 4(b). Synthesizing three sets of subimages with  $N = 5000$  particle images on each single shot took about 2 min on a desktop PC. A study of signal to noise ratio is beyond the scope of this paper, hence we do not apply any camera noise to the synthetic images.

To illustrate the working principle of SLIPI, in the present case, a constant baseline signal  $I_{DC}$  was intentionally added to the subimages on both channels to simulate multiple scattering. Three averaged SLIPI subimages corresponding to the three spatial modulation angles,  $I_0$ ,  $I_{2\pi/3}$  and  $I_{4\pi/3}$ , were generated there with the presence of uniform multiple scattering, as shown in figure 4(c).

Finally the SLIPI and the conventional images were recovered from the three subimages using equations (2) and (3).

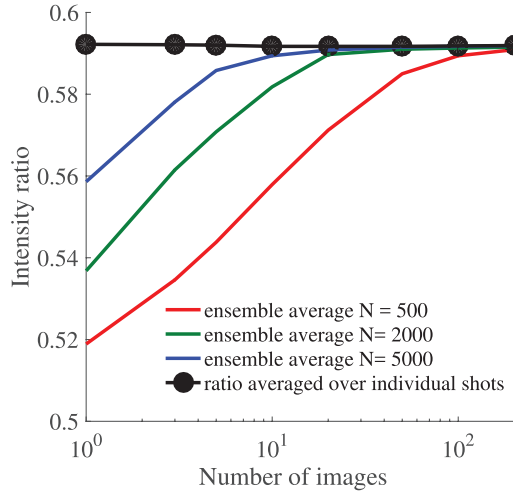


**Figure 5.** Convergence study of intensity ratio as a function of number of images averaged for SLIPI algorithm, for total particle numbers  $N = 500, 2000, 5000$  on each single image of  $200 \times 200$  pixels. Two cases are considered: in the *individual-shot averaged* case, the intensity ratio is obtained for each particle, corresponding to instantaneous SLIPI where multiple cameras are used in a single shot. In the *ensemble average* case, multiple images are averaged first before calculating the intensity ratio. In the single image case, the ratio only depends on each particle, and therefore presents a reference case for the present constant temperature field. For the ensemble averaged case, 20 images are sufficient to converge the temperature extraction when using a high seeding rate ( $N = 5000$ ).

The intensity ratio was translated into temperature by the calibration function  $R_{rb}(T, F)$ , as shown in figure 4(d). The SLIPI recovered image clearly recovers the target temperature (350 K), whilst the temperature measured without the SLIPI correction yields a biased value.

The description in figure 4 indicates the process under which SLIPI works correctly to extract the original signal. The purpose of this study is to investigate the effects of SLIPI signal retrieval on the true signal when realistic curves for phosphorescence yields are used, rather than the effectiveness of SLIPI in removing  $I_{DC}$ . Hence in the following simulations and analyses  $I_{DC}$  is set to zero.

### 3. Effect of non-linearity on signal yield

The linear behaviour of the phosphorescence signal with laser fluence is limited to a low fluence range, which followed by a slow saturation. For example, the measured linear response of BAM:Eu<sup>2+</sup> particles ends at  $2-3 \text{ mJ cm}^{-2}$ , and the corresponding emission saturates at fluences around  $200 \text{ mJ cm}^{-2}$  [14]. Similarly, the linear response limit and the saturation point for ZnO phosphorescence appears around 50 and  $250 \text{ mJ cm}^{-2}$ , respectively (see figure 3). To guarantee a robust signal to noise ratio, it is common to choose a laser fluence beyond the linear growth regime for phosphor thermography, for example  $\sim 100 \text{ mJ cm}^{-2}$  for BAM:Eu<sup>2+</sup> in [22]. However, the non-linear signal yield causes a problem for SLIPI, namely, distorted sinusoidal modulation on subimages [25] and the presence of higher order harmonics on the SLIPI reconstructed image [26]. In what follows, the effect of

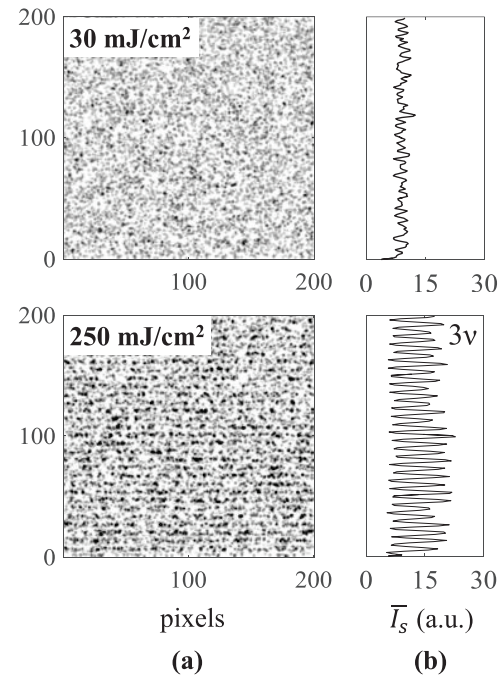


**Figure 6.** (a) Reconstructed SLIPI image on the blue channel for two selected test fluences (peak fluence). The *upper row* shows the case for  $30 \text{ mJ cm}^{-2}$  (linear regime) and the *bottom row* for  $250 \text{ mJ cm}^{-2}$  (close to saturation); (b) horizontally averaged intensity profile of the SLIPI reconstructed image. Residual noise can be observed for the case of  $250 \text{ mJ cm}^{-2}$  at a frequency of  $3\nu$ , where  $\nu$  is the spatial frequency of the Ronchi grating modulation.

non-linearity for LIP on temperature measurements is investigated. In this section, we consider a special case where the intensity ratio  $R_{rb}$  is insensitive to laser fluence, that is

$$\frac{G_r(F, T)}{G_b(F, T)} = R_{rb}(T). \quad (18)$$

This may be true for some thermographic phosphors, such as Sn-doped phosphor [27]. In contrast, for ZnO and BAM:Eu<sup>2+</sup>, the signal ratio also changes with excitation fluence, as discussed in the following section.

For this special case, the image on the blue channel was synthesized first, and the image on the red channel was then synthesized correspondingly by multiplying a constant signal ratio  $R_{rb}$  to the blue channel. Two test fluences are selected, one in the linear range (fluence  $30 \text{ mJ cm}^{-2}$ ) and the other in the saturation range ( $250 \text{ mJ cm}^{-2}$ ). The values represent the maximum fluence used in the modulated laser sheet. As expected, when a high fluence is applied, high order residual noise can be observed on SLIPI recovered image (figure 6(a) *bottom row*), whilst the noise is trivial for the low fluence case where the signal response is still in the linear regime (figure 6(a) *upper row*). The high order noise is caused by the non-harmonicity in the subsignals, and the FFT analysis shows that the frequency of this residual noise is exactly three times the ground frequency  $\nu$  (frequency of the Ronchi grating). However, since each term in equation (2) is multiplied by the same factor, the residual noise cancels out automatically when calculating the ratio between the SLIPI recovered images at the two channels:

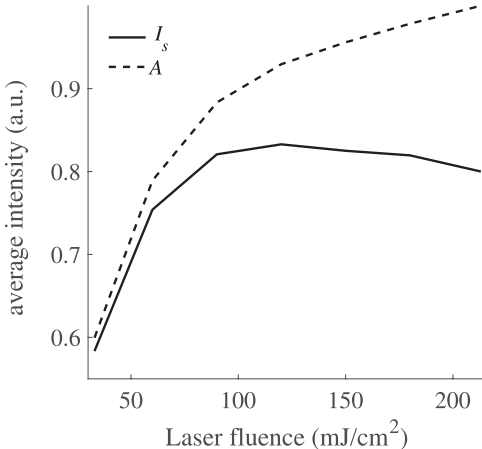


**Figure 7.**  $A$  the amplitude of true signal (dotted line) and the average intensity  $I_s$  (solid line) as a function of laser fluence on blue channel. For linear response,  $I_s$  should equal to  $A$ . However for the present non-linear response curves, a discrepancy between  $I_s$  and  $A$  is identified.

$$I_{s,r} = \sqrt{\frac{(R_{rb}I_{1,b} - R_{rb}I_{2,b})^2 + (R_{rb}I_{1,b} - R_{rb}I_{3,b})^2 + (R_{rb}I_{2,b} - R_{rb}I_{3,b})^2}{(I_{1,b} - I_{2,b})^2 + (I_{1,b} - I_{3,b})^2 + (I_{2,b} - I_{3,b})^2}} = R_{rb}. \quad (19)$$

The resulting temperature fields retrieved from simulations at both 30 and 250 mJ cm<sup>-2</sup> cases are unbiased. Although the temperature retrieval is not affected by the non-linearity in the signal response, a problem regarding the signal strength was identified during the simulation. For harmonic subsignals,  $I_s$  should be equal to the amplitude of the true signal  $A$  as denoted in equation (2), also shown in figure 2. For the present non-linear response curves, we calculate the average intensities of SLIPI recovered image under various excitation fluences and compare them with  $A$ , which is plotted in figure 7. However, a discrepancy can be observed between  $A$  and  $I_s$ , which gradually increases with excitation fluence. This is due to the fact that the SLIPI operation rejects non-linear signal gain: in essence, SLIPI acts as a spatial bandpass filter that only preserves the signal energy at the ground frequency (Ronchi grating); at high excitation fluences, the energy of non-linear signal gain is contained at frequencies other than the fundamental spatial frequency, which is removed during the SLIPI reconstruction. This has two major consequences for LIP measurements:

Firstly, when SLIPI is applied to phosphorescent emission, the signal strength of the SLIPI recovered image is reduced. In particular, this may be a severe problem for BAM:Eu<sup>2+</sup>, whose linear response ends at a very low fluence (2–3 mJ cm<sup>-2</sup>) and saturates at a very high fluence (200 mJ cm<sup>-2</sup>). The low SNR issue has been reported in [4], but was attributed to the subtraction algorithm of SLIPI subimages in that work. From the simulation presented in this study, another possible explanation seems to be that SLIPI removes the non-linear component in the signal, which represents a considerable part in phosphorescence emission from BAM:Eu<sup>2+</sup>. This creates a dilemma to the application of SLIPI to LIP: on one hand the temper-

ature bias due to multiple scattering can be successfully removed by SLIPI, on the other hand the SNR after SLIPI operation means poor precision in the temperature calculation. For ensemble-average studies, the low SNR problem can be solved by collecting more samples; for instantaneous SLIPI, however, signal boosting techniques may be necessary to overcome the low SNR problem. The issue of SNR needs to be evaluated carefully prior to the use of SLIPI on phosphor thermography.

Secondly, the removed non-linear component of the phosphorescence signal is recognized as spurious signal and labeled as multiple scattering. Consequently, the degree of multiple scattering will always be overestimated unless the signal response is in the strictly linear regime.

#### 4. Effect of intensity ratio changes to laser fluences

In the case of most frequently used thermographic phosphors such as BAM:Eu<sup>2+</sup> and ZnO, the intensity ratio is also a function of laser fluence [14, 16, 21, 24]:

$$\frac{G_r(F, T)}{G_b(F, T)} = R_{rb}(F, T). \quad (20)$$

This undesirable emission characteristic is usually avoided by using a top-hat laser sheet to obtain constant fluence, or conducting a flat-field correction at room temperature under the same flow configuration. However, to conduct SLIPI, the laser profile is intentionally modulated, so the fluence ranges from zero (ideally) to a maximum value over the test section, which may bias the measured temperature field spatially. Therefore, if the ratio of gains at the selected two channels is not constant with fluence, there could be a problem for SLIPI.

We start by considering a case where the signal remains in the linear region, for up to 30 mJ cm<sup>-2</sup>, with a spatial modulation of 20 pixels, and a constant temperature field of 350 K. No multiple scattering or camera noise was added to the synthetic images. In this case we consider the dependency of intensity ratio to the local fluence, shown in figure 8(a). Although the reconstructed SLIPI image does not show any obvious residual streaks on either channel (figure 8(b)), the modulated laser profile leaves its signature onto the temperature field (figure 8(c)), which was extracted based on the calibration curve measured at 30 mJ cm<sup>-2</sup>. The frequency of the modulation on the temperature field is  $3\nu$ , which causes a spatial temperature root mean square fluctuation of around 3 K. These streaks can be of course removed by applying low pass filters to the reconstructed SLIPI image on both channels (figure 8(d)). However, this reduces the temperature spatial resolution.

The mean temperature extracted from the SLIPI reconstructed image is 1 K higher than the target temperature, as shown in figure 8(c). However, if the laser fluence is gradually increased until the signal saturates, the temperature bias increases quickly. Figure 9 shows the temperature (spatially averaged) extracted from the SLIPI and conventional images

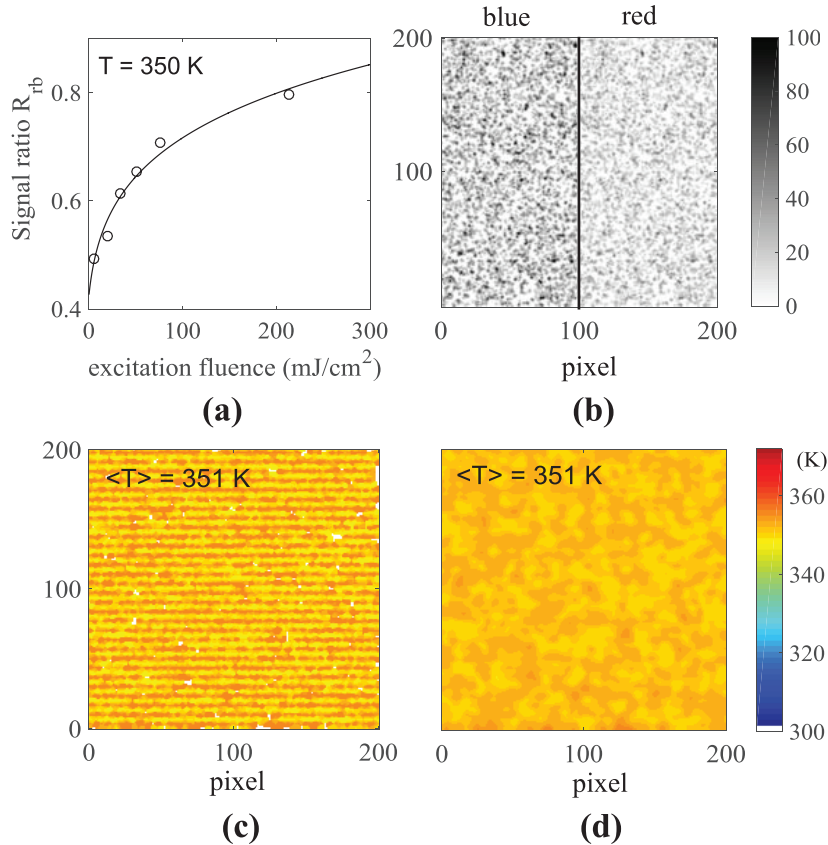


**Figure 8.** (a) Intensity ratio  $R_{rb}$  as a function of laser fluence at 350 K, based on experimental data collected from ZnO. Circles are averaged data points, and the curve is the best fit to the data points; (b) reconstructed SLIPI images for the two channels; (c) temperature field extracted from the reconstructed SLIPI images, and (d) after a low pass field was applied to (b), the streaks on temperature field are removed. For this case,  $N = 5000$ , period of modulation is 20 pixels, the laser fluence is  $30 \text{ mJ cm}^{-2}$ .

as a function of the excitation fluence, named as  $T_s$  and  $T_c$  respectively. Both  $T_s$  and  $T_c$  are biased, but towards opposite directions. The bias in  $T_s$  is explained as follows: since SLIPI removes non-linear components from the true signal, considering the signal ratio curve to laser fluences (one channel saturates faster than the other), the amount of signal removed by SLIPI from each channel is non-proportional; after subtracting the non-linear signal from the two channels, the signal ratio changes, and leads to a biased temperature measurement.

A bias in  $T_c$  of about 5 K is observed even at a low fluence values of  $\sim 30 \text{ mJ cm}^{-2}$ , where the signal response curve still appears to be quite linear (see figure 3). It suggests that the conventional images are susceptible to even slight non-linearity in the emission response, as it accumulates the error in the signal shape by adding up three subsignals. This also causes a problem in estimating the degree of multiple scattering, which is described in section 5.

Figure 9 shows the temperature bias for SLIPI using ZnO particles. BAM:Eu<sup>2+</sup>, however, yields a contrasting emission behavior to ZnO: it is a blue-shifted phosphor as temperature increases, and the red channel saturates faster than the blue channel. Hence for SLIPI performed with BAM:Eu<sup>2+</sup> particles, in theory  $T_c$  will be biased to a larger value and  $T_s$  to a smaller value.

In general, the temperature reconstruction is not affected by SLIPI for phosphors for which the signal ratio is insensitive

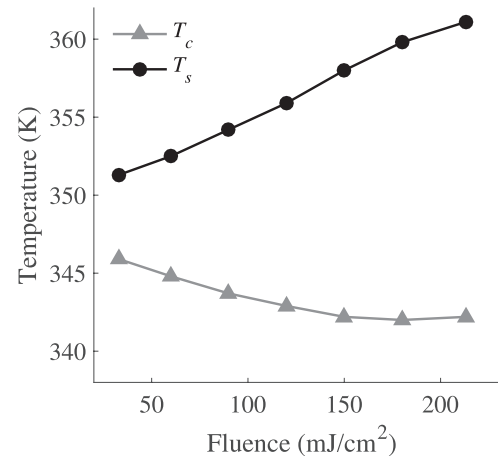


**Figure 9.** Temperature extracted from conventional ( $T_c$ ) and SLIPI images ( $T_s$ ) as a function of excitation fluence. No multiple scattering was applied to the synthetic images, so the temperature bias is purely caused by the saturating emission characteristics of ZnO. For the cases simulated in this figure,  $N = 5000$ ,  $T = 350 \text{ K}$ , and the period of modulation is 20 pixels.

to local fluence, as demonstrated in section 3. However, for those that are not, the problems described may appear. In such cases, a low excitation fluence should be selected to minimize the temperature bias. Otherwise a numerical study using the LIP-SIG program incorporated with calibration

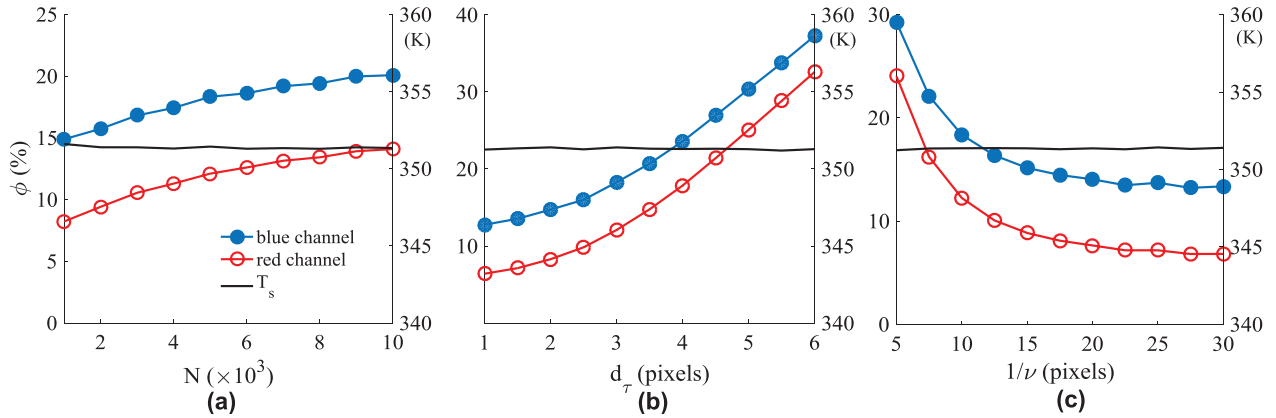


**Figure 10.** Spurious degree of multiple scattering  $\phi$  reported by SLIPI in both blue (blue circles) and red (red circles) channels for reference synthetic LIP images where zero multiple scatter signal was added, as a function of (a) particle number  $N$ , (b) particle images diameter  $d_\tau$ , and (c) period of laser sheet modulation  $1/\nu$ , respectively. For unchanged variables, excitation fluence is  $30 \text{ mJ cm}^{-2}$ , particle number  $N = 5000$ , laser sheet modulation ten pixels, and particle image diameter three pixels. The temperatures  $T_s$  extracted from the SLIPI recovered images are also plotted in the same figure on the y axis on the right side.

data acquired from a simple jet may be necessary to estimate the temperature uncertainty brought on by the application of SLIPI. For two-color fluorescence thermometry [8], a similar problem may exist if the laser fluence partially or fully saturates the fluorescent tracer. The result of SLIPI on planar droplet sizing [9] could also be affected, since Mie scattering always scales linearly with the laser fluence, whereas the fluorescence is not. Consequently, the ratio between LIF and Mie may be biased. A thorough analysis of the effects of SLIPI on LIF systems would be possible if LIF response curves were available.

## 5. Degree of multiple scattering

Kristensson and co-workers [7] used equation (4) to determine the relative amount of light being suppressed by SLIPI. In the following work by Zentgraf *et al* [4], the same equation was applied to quantify the level of multiple scattering in LIP images, and reported a very high 40% contribution to the total signal. In this study, we calculate the degree of multiple scattering on reference SLIPI subimages synthesized without multiple scattering ( $I_{DC} = 0$ ), and investigate how the signal response affects the estimation. Two reasons that may lead to an inaccurate estimate on the degree of multiple scattering are discussed as follows.

### 5.1. Overestimation caused by non-linear signal yield

As shown earlier,  $I_c$  is very sensitive to the non-harmonicity in the signal. If the signal gain is non-linear, then

$$I_c > A + I_{DC}. \quad (21)$$

This is usually the case in real experiments for both LIP and LIF. In such cases,  $(I_c - I_s)/I_c$  overestimates the degree of multiple scattering  $\phi$ . Meanwhile, part of the non-linear gain is rejected by the SLIPI operation. This further biases  $\phi$  to a higher value, since part of the true signal is recognised as multiple scattering and removed from  $I_s$ .

### 5.2. Overestimation caused by particle image diffraction

A micron-size particle usually appears larger than its physical size on the image due to diffraction. The diffraction pattern does not follow the imposed sinusoidal modulation, but instead leads to a localised blur on the intensity pattern. This effect is interpreted by SLIPI as multiple scattering. For particles of the same size  $d_p$ , we compared a case where diffraction was dominant ( $d_\tau = 4$  pixels) with a case where it was trivial ( $d_\tau = 1$  pixel), which can be achieved by changing the optical settings in a LIP experiment. Other assumed parameters were: ten pixels of modulation wavelength, a total number of 5000 particles on each single shot, a uniform temperature of 350 K, and a low laser fluence of  $30 \text{ mJ cm}^{-2}$  so as to maintain a linear signal response. After the SLIPI operation, the degree of multiple scattering for the two channels was reckoned as  $\phi_b = 23.6\%$  and  $\phi_r = 17.9\%$  for  $d_\tau = 4$  pixels; whereas for  $d_\tau = 1$  pixel,  $\phi_b = 12.8\%$  and  $\phi_r = 6.4\%$ . The disparity between the two cases is caused by the different levels of particle image diffraction. Mathematically, the overall signal on the averaged subimages no longer corresponds to a sinusoidal shape. Thus, part of the signal energy is removed by SLIPI, which further weakens the SNR of the recovered images. This comes as no surprise, because the initial purpose of the SLIPI technique was to overcome the diffraction limit in microscopic imaging and thus to achieve a theoretically unlimited resolution [26].

SLIPI removes a considerable part of the diffracted signal during the image reconstruction and subsequently yields a spurious degree of multiple scattering. This discrepancy increases with higher particle image density, larger particle image size and narrower fringes, as shown in figures 10(a)–(c), respectively. The temperature (spatially averaged) extracted from the SLIPI image for corresponding cases is also plotted in the same figure. The signal loss due to particle diffraction does not further bias the mean temperature.

The analysis on particle image diffraction also applies to SLIPI studies on dense sprays or particles. In particular, for the application of SLIPI to sprays [1], the droplet size and

concentration varies greatly in the primary and the secondary breakup zone. If SLIPI is applied to resolve the entire spray cone, the amount of true signal removed due to diffraction may be very different along the axial direction, as suggested in figures 10(a) and (b).

## 6. Simulation uncertainties

The simulation results presented in this paper illustrate how signal non-linearity affects SLIPI signal reconstruction and temperature extraction. However, for a specific experiment setup, a quantitative uncertainty analysis requires measurements (or estimations) of input parameters such as camera noise level, particle image density, particle size distribution, the relationship between particle size  $d_p$  and the strength of phosphorescence emission, and the effect of laser extinction. There are currently no direct measurements to establish the validity of each assumption, so that the specific figures predicted in this paper may be different in different SLIPI-LIP configurations, even though the general principles stated here are still valid.

Nevertheless, the goal of the SIG-LIP simulations is to provide quantitative uncertainty analysis for SLIPI-LIP experiments. Since the main focus of our investigations is the role of the non-linearity of emission in the dependence on fluence, it is important that the temperature bias predicted by the LIP-SIG program should mainly depend on the assumed or measured emission curves and excitation fluences, and only marginally on the assumptions made in section 2. Therefore, we reconsider the simulations for three cases in which the major assumptions are changed, in order to show the sensitivity of the extracted temperature to them: (a) the emission intensity is proportional to either  $d_p^2$  or  $d_p^3$  (in both cases with  $d_p$  following a lognormal distribution, whilst in the previous simulations it was assumed to be monodisperse); (b) the particle image intensity distribution  $I_p$  follows a top-hat rather than a Gaussian profile; and (c) the particle image size  $d_\tau$  is not constant over the simulation area, but rather follows a normal distribution. In theory,  $d_\tau$  can be calculated from the  $d_p$  distribution in case (a), by incorporating relevant optical settings [23]. However, since the particle size range considered here belongs to a diffraction-limited case, the variation of  $d_p$  causes little change in  $d_\tau$ . So instead we add a distribution to  $d_\tau$  directly. The main reason for the choice of the three parameters above is that they are often difficult to measure in real LIP experiments.

$T_s$  curves in figure 9 are reproduced for the three variant cases considered, and the results are plotted in figure 11. The distributions of  $d_p$  and  $d_\tau$  are plotted in the subfigures accordingly. The changes in the dependence of the intensity with diameter affect the recovered temperature at high fluences (figure 11(a)). If  $I_p \propto d_p^3$ , more signal is contributed by large particles located in high fluence regions, which slightly increases the proportion of saturated signal. The changes in the particle image profile (Gaussian versus top-hat) also alter the energy distribution on the frequency domain, leading to a slight disparity in  $T_s$  at high laser fluences (figure 11(b)).

Finally, changes in  $d_\tau$  do not change the final temperature significantly (figure 11(c)), as the temperature depends on the ratio of quantities. Clearly, for all three cases, using these different assumptions causes very small differences in the recovered temperatures. In the worst case scenario, case (b) at 210 mJ cm<sup>-2</sup>, the disparity in  $T_s$  is still lower than 2 K. The results demonstrate again the major advantage of intensity-ratio methods: factors that may affect the absolute intensity cancel out automatically, leaving primarily the spectrum shift to play its role on temperature extraction.

## 7. Possible applications of the LIP-SIG program

As illustrated, there are several possible applications of the modified LIP-SIG program, as follows.

Firstly, the LIP-SIG program can provide guidance to experimentalists performing SLIPI regarding errors and convergence. Figure 5 shows that at least 20 images must be averaged to achieve convergence for 5000 particles per single shot (0.125 particles/pixel). If a particle seeding density below this level is used, more images should be acquired to converge the SLIPI calculation, which can be predicted by the LIP-SIG program.

Secondly, the simulations allow the estimation of the expected degree of multiple scattering in LIP images. As demonstrated earlier, due to non-linear signal gain and particle diffraction, SLIPI overestimates the contribution from multiple scattering in real experiments. The LIP-SIG program can show how much of the true signal will be removed during the SLIPI operation, by synthesizing noise-free reference SLIPI subimages under the same test conditions with experimental calibration data. The true degree of multiple scattering can then be determined by subtracting the spurious degree of multiple scattering  $\phi$  from the measured value.

Thirdly, the simulations allow an assessment of the temperature bias caused by SLIPI. If the emission spectrum of phosphor particles is sensitive to the excitation fluence, the measured temperature may be biased by the SLIPI operation, especially for cases with a high laser fluence. In such cases, the LIP-SIG program can help identify the potential temperature bias for the test condition, which can be used to correct the measured value or to facilitate an uncertainty analysis.

Fourthly, it becomes possible to investigate preferential re-absorption. The signal spectrum from the measurement plane is irreversibly changed by re-absorption before it reaches the detector, which in principle cannot be corrected by SLIPI. If changes in the intensity ratio introduced by low SNR and non-linear signal yield have been estimated by LIP-SIG and eradicated from the measured value, the remaining discrepancy in the intensity ratio measured in a low-seeding and a high-seeding (with SLIPI) case should, in principle, be due to the preferential re-absorption. This discrepancy should also show a correlation to the local temperature. Since changes in local temperature shift the emission spectrum, the overlapping wavelength band will either be broadened or narrowed, which then amplifies or suppresses the preferential re-absorption. Demonstrating the correlation between residual temperature

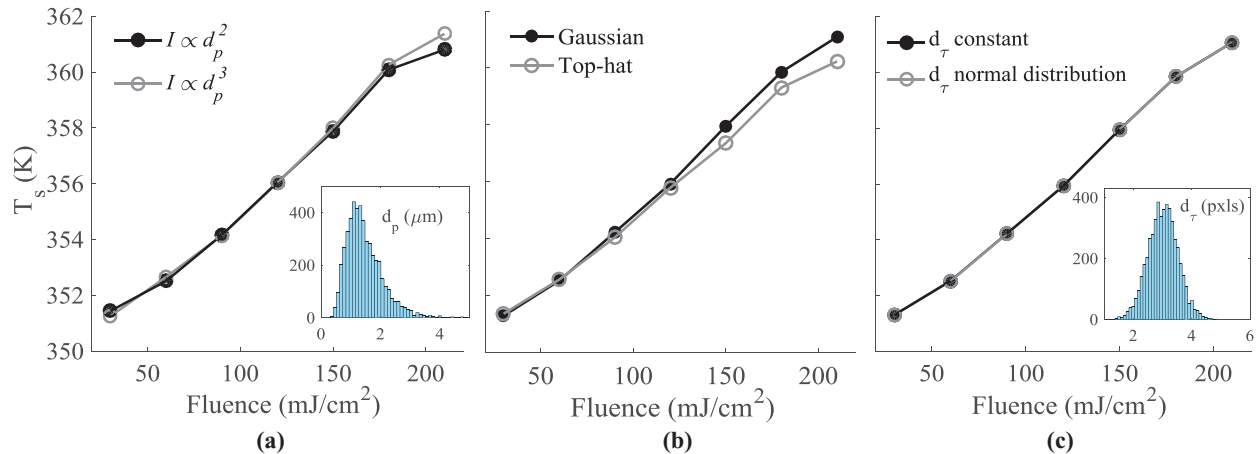


**Figure 11.** SLIPI recovered temperature  $T_s$  from a uniform field as a function of excitation fluence, for (a) an emission intensity in proportionality to  $d_p^2$  or  $d_p^3$ ;  $d_p$  with a lognormal distribution with 2  $\mu\text{m}$  SMD and a 0.4  $\mu\text{m}$  standard log deviation; (b) a Gaussian or top-hat particle image profile; (c) a constant or a varying particle image size  $d_\tau$  over the simulation field. For the latter case,  $d_\tau$  follows a normal distribution. The mean particle image size is three pixels and the standard deviation is 0.5 pixel. Unless stated, other parameters are kept the same as figure 9.

bias and spectrum shift experimentally on both ZnO and BAM:Eu<sup>2+</sup>, with the help of LIP-SIG program, can be a strong proof of the existence of preferential re-absorption.

Finally, the same procedure can allow an estimation of PIV uncertainty which would result from the use of fluorescent tracers. The LIP-SIG program can be easily adapted to simulate fluorescent particles as velocity tracers, which have been widely applied in micro-PIV for biological studies. This can be used to investigate the effects such as out-of-focus particle images on the measurement accuracy, which is a common problem for micro-PIV because the imaging system for this application usually has a very narrow depth of field.

## 8. Conclusions

This study investigates the potential effects that structured laser illumination planar imaging (SLIPI) may have on the accuracy of gas-phase phosphor thermography. A LIP-SIG program is developed and combined with signal yield functions obtained from experimental data with ZnO to generate artificial LIP images. The SLIPI process is simulated by generating LIP images under sinusoidally modulated laser sheets, and then recovering the target temperature field from these images. The main findings are summarized as follows:

- For phosphor particles whose emission strength scales non-linearly with the excitation fluence, the sinusoidal modulation is distorted on each subimage. This leaves higher order residual noise on the SLIPI reconstructed image  $I_s$ . However, if the signal ratio does not change with laser fluence, the residual noise cancels out automatically when calculating the signal ratio from two channels, and hence does not affect the temperature retrieval.
- When the phosphorescent emission is close to saturation, a substantial amount of true signal energy is removed by the SLIPI operation, because the energy of non-linear

signal gain transfers from the ground frequency to other spatial frequencies, which is recognised as undesired signal by SLIPI.

- A complicating situation appears for phosphors whose intensity ratio changes with the excitation fluence, for example ZnO and BAM:Eu<sup>2+</sup>. Residual streaks appear on the recovered temperature field. This can be removed by applying a low-pass filter to the SLIPI reconstructed images which, however, reduces the spatial resolution.
- The mean temperature after SLIPI operation can also be affected by the intensity ratio changes due to modulated laser sheets. If a low fluence is applied to keep the emission in the linear range, the temperature bias is trivial. However, when using high laser fluences ( $\sim 200 \text{ mJ cm}^{-2}$ ), a larger temperature bias can appear.
- The SLIPI operation is very likely to overestimate the degree of multiple scattering in LIP images, because the non-linear signal yield and particle diffraction are not sinusoidal-modulated, but are identified as multiple scattering by SLIPI. This may occur in SLIPI with LIF and with Mie scattering (particle-based) as well.

Future work will focus on conducting SLIPI-LIP experiments in a well-controlled environment such as in a laminar air jet or in water [27, 28], and comparing the results with those predicted by the LIP-SIG program. After experimental validation, the program can be applied to investigate more complex scenarios such as two-pulse and one-pulse SLIPI on phosphor thermometry.

## Acknowledgments

The authors gratefully acknowledge the informal discussions with Prof Frank Beyrau, Dr Benoit Fond, and Mr Zentgraf, as well as the help from Prof Jerry Westerweel and Mr Dante McGrath. The project has been partly funded by the Universiti Teknologi Malaysia, under Grant Number RG84263.

## ORCID iDs

Luming Fan  <https://orcid.org/0000-0002-9856-4853>  
 Simone Hochgreb  <https://orcid.org/0001-7192-4786>

## References

- [1] Berrocal E, Kristensson E, Richter M, Linne M and Aldén M 2008 Application of structured illumination for multiple scattering suppression in planar laser imaging of dense sprays *Opt. Express* **16** 17870–81
- [2] van Lipzig J P J, Yu M, Dam N J, Luijten C C M and de Goeij L P H 2013 Gas-phase thermometry in a high-pressure cell using BaMgAl10O17:Eu as a thermographic phosphor *Appl. Phys. B* **111** 469–81
- [3] Lee H, Böhm B, Sadiki A and Dreizler A 2016 Turbulent heat flux measurement in a non-reacting round jet, using BAM:Eu<sup>2+</sup> phosphor thermography and particle image velocimetry *Appl. Phys. B: Lasers Opt.* **122** 1–13
- [4] Zentgraf F, Stephan M, Berrocal E, Albert B, Böhm B and Dreizler A 2017 Application of structured illumination to gas phase thermometry using thermographic phosphor particles: a study for averaged imaging *Exp. Fluids* **58** 1–15
- [5] Stephan M, Lee H, Albert B, Dreizler A and Böhm B 2016 Simultaneous planar gas–phase temperature and velocity measurements within a film cooling configuration using thermographic phosphors *18th Int. Symp. on the Application of Laser and Imaging Techniques to Fluid Mechanics*
- [6] Abram C, Fond B and Beyrau F 2018 Temperature measurement techniques for gas and liquid flows using thermographic phosphor tracer particles *Prog. Energy Combust. Sci.* **64** 93–156
- [7] Kristensson E, Araneo L, Berrocal E, Manin J, Richter M, Aldén M and Linne M 2011 Analysis of multiple scattering suppression using structured laser illumination planar imaging in scattering and fluorescing media *Opt. Express* **19** 13647
- [8] Mishra Y N, Nada F A, Polster S, Kristensson E and Berrocal E 2016 Thermometry in aqueous solutions and sprays using two-color LIF and structured illumination *Opt. Express* **24** 4949–63
- [9] Mishra Y N, Kristensson E and Berrocal E 2014 Reliable LIF/Mie droplet sizing in sprays using structured laser illumination planar imaging *Opt. Express* **22** 4480
- [10] Kristensson E, Ehn A, Bood J and Aldén M 2015 Advancements in Rayleigh scattering thermometry by means of structured illumination *Proc. Combust. Inst.* **35** 3689–96
- [11] Kristensson E, Berrocal E and Aldén M 2014 Two-pulse structured illumination imaging *Opt. Lett.* **39** 2584–7
- [12] Mishra Y N, Kristensson E, Koegl M, Jönsson J, Zigan L and Berrocal E 2017 Comparison between two-phase and one-phase SLIPI for instantaneous imaging of transient sprays *Exp. Fluids* **58** 1–17
- [13] Kristensson E and Berrocal E 2018 Crossed patterned structured illumination for the analysis and velocimetry of transient turbid media *Sci. Rep.* **8** 1–9
- [14] Fond B, Abram C and Beyrau F 2015 Characterisation of the luminescence properties of BAM:Eu<sup>2+</sup> + particles as a tracer for thermographic particle image velocimetry *Appl. Phys. B* **121** 495–509
- [15] Hertle E, Will S and Zigan L 2017 Characterization of YAG:Dy,Er for thermographic particle image velocimetry in a calibration cell *Meas. Sci. Technol.* **28** 025013
- [16] Abram C, Pougin M and Beyrau F 2016 Temperature field measurements in liquids using ZnO thermographic phosphor tracer particles *Exp. Fluids* **57** 1–14
- [17] Storch M, Mishra Y N, Koegl M, Kristensson E, Will S, Zigan L and Berrocal E 2016 Two-phase SLIPI for instantaneous LIF and Mie imaging of transient fuel sprays *Opt. Lett.* **41** 5422
- [18] Lecordier B and Westerweel J 2004 The EUROPIV synthetic image generator (S.I.G.) *Particle Image Velocimetry: Recent Improvements* (Berlin: Springer) pp 145–61
- [19] Sciacchitano A, Wieneke B and Scarano F 2013 PIV uncertainty quantification by image matching *Meas. Sci. Technol.* **24** 045302
- [20] Wieneke B 2015 PIV uncertainty quantification from correlation statistics *Meas. Sci. Technol.* **26** 74002
- [21] Fan L, Gao Y, Hayakawa A and Hochgreb S 2016 Simultaneous, two-camera, 2D gas-phase temperature and velocity measurements by thermographic particle image velocimetry with ZnO tracers *Exp. Fluids* **58** 1–12
- [22] Fond B, Abram C, Heyes A L, Kempf A M and Beyrau F 2012 Simultaneous temperature, mixture fraction and velocity imaging in turbulent flows using thermographic phosphor tracer particles *Opt. Express* **20** 22118–33
- [23] Adrian R J and Yao C S 1985 Pulsed laser technique application to liquid and gaseous flows and the scattering power of seed materials *Appl. Opt.* **24** 44–52
- [24] Witkowski D and Rothamer D A 2018 Investigation of aerosol phosphor thermometry (APT) measurement biases for Eu:BAM *Appl. Phys. B* **124** 202
- [25] Kristensson E 2012 Structured laser illumination planar imaging SLIPI applications for spray diagnostics *Dissertation Lund University*
- [26] Gustafsson M G L 2005 Nonlinear structured-illumination microscopy: wide-field fluorescence imaging with theoretically unlimited resolution *Proc. Natl Acad. Sci.* **102** 13081–6
- [27] Fond B, Abram C, Pougin M and Beyrau F 2019 Investigation of the tin-doped phosphor (Sr,Mg)<sub>3</sub>(PO<sub>4</sub>)<sub>2</sub>:Sn<sup>2+</sup> for fluid temperature measurements *Opt. Mater. Express* **9** 802
- [28] Fond B, Abram C, Pougin M and Beyrau F 2019 Characterisation of dispersed phosphor particles for quantitative photoluminescence measurements *Opt. Mater.* **89** 615–22